
Since January 2020 Elsevier has created a COVID-19 resource centre with free information in English and Mandarin on the novel coronavirus COVID-19. The COVID-19 resource centre is hosted on Elsevier Connect, the company's public news and information website.

Applied Surface Science 533 (2020) 147516

Contents lists available at ScienceDirect

Applied Surface Science

journal homepage: www.elsevier.com/locate/apsusc

# Electrospun antibacterial poly(vinyl alcohol)/Ag nanoparticles membrane grafted with 3,3′,4,4′-benzophenone tetracarboxylic acid for efficient air filtration

Siying Li[a,1], Rong Zhang[a,1], Junlan Xie[a], Dur E. Sameen[a], Saeed Ahmed[a], Jianwu Dai[b], Wen Qin[a], Suqing Li[a], Yaowen Liu[a,c,d,*]

[a] College of Food Science, Sichuan Agricultural University, Yaan 625014, China
[b] College of Mechanical and Electrical Engineering, Sichuan Agricultural University, Ya'an 625014, China
[c] California NanoSystems Institute, University of California, Los Angeles, CA 90095, USA
[d] Department of Bioengineering, University of California, Los Angeles, CA, 90095, USA

ARTICLE INFO

*Keywords:*
Poly(vinyl alcohol)
Ag nanoparticles
3,3′,4,4′-Biphenyltetracarboxylic acid
Reactive oxygen species
Antibacterial

ABSTRACT

In this study, poly(vinyl alcohol) (PVA) membranes containing Ag nanoparticles (AgNPs) were prepared by electrospinning and grafted copolymerization with 3,3′,4,4′-benzophenone tetracarboxylic acid (BPTA) to provide better mechanical properties, lower water vapor transmittance, and higher antibacterial activity (against *Staphylococcus aureus* and *Escherichia coli*) than the PVA/AgNPs membrane. The PVA/AgNPs/BPTA membrane showed higher antibacterial activity than the other membranes, and it produced inhibition zones with diameters of 18.12 ± 0.08 and 16.41 ± 0.05 mm against *S. aureus* and *E. coli*, respectively. The PVA/AgNPs/BPTA membrane was found to be capable of promoting reactive oxygen species (ROS) formation under both light and dark conditions. Cycling experiments performed following ROS quenching showed that the best-performing composite membrane retained > 70% of its original OH· radical and $H_2O_2$ charging capacity after seven cycles. In the filtration test, the electrospun nanofibrous membranes showed high filtration efficiencies of 99.98% for sodium chloride (NaCl). In addition, these membranes maintained a relatively low pressure drop of 168 Pa with a basis weight of 2.1 g $m^{-2}$. Thus, the PVA/AgNPs/BPTA membrane was concluded to be a promising medical protective material offering the benefits of structural stability and reusability.

## 1. Introduction

The recent outbreak of pneumonia caused by the SARS-CoV-2 virus resulted in a public health emergency and thus became a matter of global concern [1]. Under such circumstances, healthcare workers directly contacting infected patients have to wear full medical protective equipment (e.g., disposable medical protective clothing) to prevent human-to-human virus transmission, which has caused a shortage of such equipment and highlighted the need for novel medical barrier fabrics with higher durability and reusability.

Eco-friendly fibrous materials for environmental air filtration can be designed to feature high filtration efficiency, high tensile strength, biocompatibility, and antibacterial properties [2]. Many of these materials contain poly(vinyl alcohol) (PVA), which is commonly processed by electrospinning, features the advantages of non-toxicity, mechanical stability, biocompatibility, and excellent film-forming ability, and is extensively used as a component of air filtration devices, medical supplies, and food packaging [3]. Bioprotective materials typically contain metal nanoparticles, nanocellulose, and chitosan as antibacterial constituents [4]. Specifically, the antibacterial activity of biomedical products such as wound dressings, hydrogels, membranes, and fibers is commonly enhanced by supplementation with photoactive Ag nanoparticles (AgNPs) [5], which kill microorganisms by (i) gradually releasing $Ag^+$ ions to hinder ATP production and DNA replication, (ii) directly destroying cell membranes, and (iii) promoting the generation of reactive oxygen species (ROS) [6]. However, owing to the irreversible consumption of fungicides, their direct bactericidal action usually decreases significantly with the length and number of times they are used [7].

Photocatalysts and photosensitizers have attracted considerable

* Corresponding author at: College of Food Science, Sichuan Agricultural University, Yaan 625014, China.
*E-mail address:* lyw@my.swjtu.edu.cn (Y. Liu).
[1] These authors contributed equally to the work.

https://doi.org/10.1016/j.apsusc.2020.147516
Received 29 June 2020; Received in revised form 31 July 2020; Accepted 7 August 2020
Available online 13 August 2020
0169-4332/ 

attention as photoactive antibacterial agents with high antibacterial activity, good controllability, low toxicity, and high efficiency. The antibacterial function of photosensitive compounds can be triggered and controlled by irradiation with UV-A or visible light (λ = 320–700 nm) [8]. For example, inorganic photosensitizers (such as $TiO_2$, $Fe_2O_3$ and ZnO) can be physically embedded in textiles or films, but photosensitive substances may be released from their matrix, which will shorten the life of these functional materials [9]. Organic materials with photoinduced antimicrobial activity, e.g., benzophenone-derivative-containing fibers [10], exhibit strong bactericidal effects but are driven by high-energy UV light rather than by readily available sunlight. The antibacterial activity of certain photoactive chemicals can be triggered and controlled by near-UV to visible-range light (300–700 nm) [11]. In particular, 3,3′,4,4′-benzophenone tetracarboxylic acid (BPTA) can effectively impart photoinduced antibacterial activity, as exemplified by the excellent antibacterial performance of BPTA-treated cotton cellulose [12]. In view of the lower pH and higher anion concentration in the reaction system compared to those of other photosensitive substances, esterification efficiency can be increased by lowering the $pK_a$ of the corresponding acid in the catalyst. Sodium hypophosphite, a salt with moderate acidity and small anion size, has proven to be a good esterification catalyst [13]. The two anhydride groups of BPTA can be hydrolyzed to afford the corresponding tetracarboxylic acid (BPTCA), which is soluble in hot water. Notably, BPTCA aqueous solutions can be directly used in fiber membrane processing and react with hydroxyl groups in the presence of sodium hypophosphite as a catalyst to form esters [11,13]. The ability of BPTA to promote ROS (e.g., HO· and $H_2O_2$) generation both upon irradiation with light and under dim light/dark conditions results in “always-on” bactericidal activity, as the thus produced ROS rapidly destroy DNA, RNA, proteins, and lipids to induce bacterial death and virus inactivation [11,14]. Polymer nanocomposites are superior functional materials comprising nanoparticles coated on a polymer matrix or dispersed therein [15]. For example, silvered BPTA dianhydride and 4,4'-oxydianiline polyimide films prepared by casting monophasic homogeneous Ag(I) perfluorocarboxylate–poly solutions on glass exhibit outstanding mirror reflectance, surface conductivity, and metal-polymer bonding while retaining the essential mechanical properties of native polyimide [16]. In another work, hierarchical nanostructures obtained by surface-constrained synthesis of AgNPs on electrospun BPTA/AAPTMI/polyimide nanofibers were probed by X-ray diffraction (XRD) analysis and elemental mapping images to confirm the existence of the Ag phase and the chemical modification of the polymer matrix, respectively [17]. At this point, it should be noted that the good ability of PVA to cap AgNPs makes it a better choice for the above blend.

Herein, PVA/AgNPs composite nanofibrous membranes were fabricated by electrospinning, which is an excellent technique for preparing nanocomposite membranes with a large surface area-to-volume ratio and three-dimensional open structure [18]. Subsequent BPTA grafting was conducted by immersing the membranes in variable-concentration BPTA solutions and relied on the sodium-hypophosphite-catalyzed esterification of BPTA carboxyl groups with hydroxyl groups [11]. By studying the specific ROS content produced by Ag NPs and BPTA under visible and dark light conditions, the reactive oxygen species were easy to be released under various conditions and the nanofiber membrane had repeatable bactericidal activity, and the mechanism of the light-induced benzophenone group was discussed. Finally, the antibacterial, air filtration, and bioprotection capabilities of PVA/AgNPs/BPTA composite membranes were investigated, the inhibition rate of *E. coli* in the experimental sample always exceeded 90%, better than the N95 mask.

## 2. Material and methods

### 2.1. Materials

PVA (polymerization degree = 1750 ± 50, alcoholysis degree = 98–99%) and BPTA were purchased from Shanghai Aladdin Biochemical Technology Co., Ltd. AgNPs with an average particle size of 20 nm were purchased from Shanghai Chaowei Nano Co. N,N-dimethyl-4-nitrosoaniline (p-NDA) and 2,2-diphenyl-1-picrylhydrazyl (DPPH) were acquired from Sigma-Aldrich (St. Louis, MO, USA). All other chemicals and solvents were analytical grade and obtained from Chengdu Kelong Reagent Co. (Chengdu, China), unless otherwise indicated.

### 2.2. Preparation of PVA/AgNPs nanofibrous membranes

PVA/AgNPs nanofibrous membranes were fabricated by electrospinning. Briefly, AgNPs (0.5 g) were dispersed in deionized water (2 mL) for 1 h using a 50-W ultrasonic bath (Shanghai Keqi Instrument Equipment Co., Ltd., KQ100DE). In another beaker, PVA (10 wt%) was dissolved in deionized water (8 mL) at 95 °C for 2 h, and the obtained solution was supplemented with that of AgNPs. The resulting mixture was vigorously stirred using a magnetic stirrer for 10 h at room temperature to obtain a homogenous precursor solution with PVA and AgNPs contents of 10 and 1 wt%, respectively, and then sonicated [19].

The prepared PVA/AgNPs solution was placed in a 10-mL plastic syringe with a 0.7-mm-diameter needle and extruded at 0.010 mL $min^{-1}$ using a syringe pump. This syringe was horizontally fixed on the syringe pump, and the metal needle tip was connected to the electrode of a high-voltage power supply held at 15 kV. PVA/AgNPs fibrous membranes were collected as overlaid membranes on electrically grounded Al foil, which covered a roller collector plate placed 12 cm away from the needle tip at ambient temperature (25 °C). After 10 mL of the solution had been consumed, the collector with the PVA/AgNPs fibrous membrane was dried overnight at 25 °C.

### 2.3. Catalytically grafted BPTA

In anticipation that the combination of metal nanoparticles and benzophenone might synergistically affect photoactivity, PVA/AgNPs membranes were further grafted with BPTA to obtain PVA/AgNPs/BPTA nanofibrous membranes [20]. Specifically, BPTA was dissolved in distilled water at concentrations of 10, 30, 50, and 70 g $L^{-1}$ upon stirring at 70–80 °C, and the solution was supplemented with sodium hypophosphite monohydrate (catalyst) to afford a catalyst: BPTA ratio of 1:2 (mol/mol) [21]. After a 2-h immersion in the above solution, the membranes were washed with acetone and dried under vacuum.

### 2.4. Membrane characterization

The morphology, surface chemical composition, thermal behavior, and crystallinity of membranes were characterized. A scanning electron microscope (FEI Quanta200, the Netherlands) equipped with a field-emission gun and a Robinson detector operating at an acceleration voltage of 10 kV was used to observe the membrane morphology. Prior to imaging, samples were sputter-coated with a thin layer of Au.

The surface chemical compositions of pure materials and nanocomposites were probed by attenuated total reflectance FTIR spectroscopy (Bruker Gmbh, Ettlingen, Germany). Samples were placed directly on the sensor of the FTIR-ATR spectrometer, and spectra were recorded in the wavenumber range of 650–4000 $cm^{-1}$ at a resolution of 4 $cm^{-1}$ and a scan speed of 32 $s^{-1}$.

To examine the thermal properties of films, differential scanning calorimetry (DSC) (STA 449C, Netsch, Germany) measurements were conducted under flowing nitrogen within 50–350 °C at a heating rate of 10 °C $min^{-1}$ [22]. Approximately 1–2 mg samples were first

conditioned in hermetic aluminum pans.

The elemental compositions of the Au-coated samples were analyzed using an energy dispersive X-ray analysis (EDAX) (Model: Octane Plus), that was connected with SEM. Thus, the EDAX spectra of ceramic samples were recorded by scanning a selected area of the specimen with the electron beam. The overall crystallinity of the composite fibrous membranes was probed by powder XRD (MPX3, MAC Science, Japan). Four identical membrane samples (2 × 2 cm) were stacked and placed directly on the radiation exposure stage to record XRD patterns within a 2θ range of 5–80° at a scan step of 0.4° $min^{-1}$, voltage of 40 kV, and current of 50 mA.

### 2.5. Thickness and mechanical properties of membranes

The membrane thickness was measured using a hand-held digital thickness gauge (Check Line DCN-900, USA) with an accuracy of 0.001 mm at different sample points (at the center and around edges). The average values of 10 datasets were computed to check sample thickness uniformity [23].

The tensile strength (TS) and elongation at break (EB) were measured using an HD-B609B-S tensile tester (Haida International Equipment Co., Ltd.) according to the methods of Wang et al [24]. Each membrane was cut into 60 × 10 mm rectangular strips that were stretched at 50 mm $min^{-1}$. Experiments were conducted in triplicate for both TS and EB measurements.

### 2.6. Surface color of membranes

The color of the membranes was measured at randomly selected points by a chromometer (Konica Minolta, CR-400, Tokyo, Japan) using a standard white plate as a background and expressed in terms of L* (brightness), a* (red-green intensity), and b* (yellow-blue intensity) [25]. The total color difference (ΔE*) was then calculated according to Eq. (1):

$$\Delta E* = [(\Delta a*)^2 + (\Delta L*)^2 + (\Delta b*)^2]^{0.5} \quad (1)$$

where $\Delta L^*$, $\Delta a^*$, and $\Delta b^*$ are the differences between the color values of the standard color plate and studied membranes.

### 2.7. Moisture content (MC) and swelling degree (SD)

Samples were pre-weighed and oven-dried to an equilibrium weight at 105 °C [26], and the MC was calculated with Eq. (2):

$$MC = \frac{W_\omega - W_d}{W_\omega} \times 100\% \quad (2)$$

where $W_\omega$ is the initial equilibrium weight of the membrane stored at room temperature, and $W_d$ is the membrane weight after drying. Three samples per membrane were tested to measure the average MC.

For swelling behavior characterization, membranes were immersed in distilled water (50 mL) at 37 °C for 24 h [26]. As PVA1799 is insoluble in water, we only calculated the membrane SD using Eq. (3):

$$SD = \frac{W_s - W_d}{W_d} \times 100\% \quad (3)$$

where $W_s$ is the film weight after soaking for 24 h and removing the surface water with blotting paper, and $W_d$ is the final weight of the membranes after drying for 24 h.

### 2.8. Water vapor permeability (WVP)

The WVP was determined gravimetrically according to a slight modification in the ASTM standard test method (ASTM, 2003). The membranes (3 × 3 cm) were sealed in glass test tubes containing silica gel (0% relative humidity (RH)) and then stored in a desiccator that was filled with distilled water (100% RH) at 25 °C and 53% RH and sealed to prevent water vapor leakage. The test tubes were weighed every three days over a period of 15 days. Measurements were conducted in triplicate for each membrane sample, and WVP was calculated according to Eq. (4) [27]:

$$WVP = \frac{\Delta w}{t} \times \frac{x}{A \times \Delta P} \quad (4)$$

where $\Delta w$ is the weight change (g), $t$ is time (h), $x$ is the membrane thickness (m), $A$ is the membrane sample area ($m^2$), and $\Delta P$ (kPa) is the vapor pressure difference across the membrane at 25 °C.

### 2.9. ROS quantitation

To test the photoactivity of composite membranes, we determined the yields of two typical ROS (OH· and $H_2O_2$) under daylight irradiation simulated using a D65 standard daylight tube (GE F15T8/D). Hydroxyl radicals generated by BPTA-treated composite membranes were quantified by an indirect spectrophotometric method using *p*-NDA as an OH·-selective scavenger [28]. In a typical test, a 10-mg membrane sample was immersed in a solution of *p*-NDA (50 mM, 10 mL) and exposed to the D65 standard light source or dark conditions for a certain time. The concentration of residual *p*-NDA was determined from the absorbance at 440 nm [7]. To quantify the amount of released OH· radicals, a p-NDA calibration curve in $H_2O$ was constructed and used to certify *p*-NDA concentration prior to irradiation ($C_0$). After light exposure, the absorbance of the *p*-NDA solution was measured to obtain the residual concentration ($C_1$) and hence the amount of consumed *p*-NDA. Hydroxyl radicals oxidized *p*-NDA to afford an intermediate that underwent disproportionation to afford equal amounts of a nitro species (not absorbing at 440 nm) and *p*-NDA, which allowed one to calculate the amount of produced OH· radicals.

$H_2O_2$ produced over composite membranes was quantified by the method reported by Hou et al. and another indirect spectrophotometric method detailed in the Standard Operating Procedure: Procedure for Analyzing Hydrogen Peroxide Concentrations in Water (Procedure No: GSI/SOP/BS/RA/C/7, Issue Date: June 15, 2009) [14]. A 5-mg membrane sample was placed in deionized water (5 mL) and exposed to daylight or dark conditions for a certain time. After exposure, a 1-mL solution aliquot was mixed with 1 mL of reagent I [aqueous solution of KI (66 g $L^{-1}$), NaOH (2 g $L^{-1}$), and $(NH_4)_6Mo_7O_{24}{\cdot}4H_2O$ (0.2 g $L^{-1}$)] and 1 mL of reagent II [aqueous solution of potassium hydrogen phthalate (20 g $L^{-1}$)] upon 10-min stirring. The concentration of $H_2O_2$ was determined from the absorbance at 351 nm using a calibration curve to obtain the $H_2O_2$ production capacity of the composite membrane.

### 2.10. Antioxidant activity evaluation

Antioxidant activity was determined by the DPPH radical scavenging assay. In a typical test, a 0.1-g membrane sample was extracted with methanol (2.5 mL), 100 μL of the sample extract was added to 4.9 mL of 0.1 mM methanolic DPPH upon vortex mixing, and the mixture was incubated at 25 °C for 30 min in the dark [27]. Changes in the extract absorbance at 517 nm were measured using a UV–vis spectrophotometer. Five tests were performed for each sample, and the obtained averages were used to calculate the antioxidant activity with Eq. (5):

$$DPPHscavengingactivity = \frac{(ADPPH - AS)}{ADPPH} \times 100\% \quad (5)$$

where $A_{DPPH}$ is the original absorbance of methanolic DPPH, and $A_s$ is the absorbance of the DPPH assay solution.

### 2.11. Antimicrobial activity evaluation

To probe the antibacterial properties of neat PVA and composite

membranes, we analyzed their ability to inhibit the growth of two foodborne pathogens, namely gram-positive *S. aureus* (*S. aureus PTCC 1112)* and gram-negative *E. coli* (*E. coli PTCC1270*), using a disk inhibition method. *E. coli* and *S. aureus* were aseptically inoculated in trypticase soy broth and shake-cultured at 37 °C for 24 h [29]. Lysogeny broth agar was used as a bacterial growth medium. The bacterial culture (0.2 mL, $10^6$ CFU $mL^{-1}$) was uniformly dispersed on the plate medium surface [30]. The membranes were cut into 8-mm-diameter circles and placed on the upper layer of agar plates, which were then incubated at 37 °C for 24 h. The widths of the inhibition zone formed around the membranes were considered as a measure of the antibacterial activity. All samples were characterized in triplicate.

### 2.12. Air filtration performance

Using the method of intercepting sodium chloride (NaCl) aerosol particles, a filter material comprehensive performance tester (LZC-H) was used to study the performance of membranes for intercepting ultrafine particles. The average diameter of the dispersed solid mass, in this case 300–500 nm neutral single NaCl particles, was used to evaluate the aerosol filtration performance under increased airflow. The filter QF values are used to measure the relationship between the filter efficiency and pressure drop, which was calculated using Eq. (6):

$$QF = -\frac{\ln(1-\eta)}{\Delta P} \tag{6}$$

where η is the filtration efficiency, and $\Delta P$ is the pressure drop.

In addition, a $1 \times 10^6$ cfu aerosol containing *E. coli* was prepared as a model infection aerosol, the size of which was similar to that of aerosols produced by human sneezing or coughing. PVA/AgNPs/BPTA-50 g $L^{-1}$, with dimensions of $3 \times 3$ $cm^2$, was attached to the right side of the 3 M N95 mask, and irradiated for 1 h, and the respirator was exposed to an aerosol flow of 0.2 mL $min^{-1}$ for 30 s. A dust mask without antibacterial properties was used as a control. After standing for 30 min, three groups of live bacteria were collected and measured in the control area, sample area and N95 area. The experiment was repeated seven times.

### 2.13. Statistical analysis

The results were reported as mean ± standard deviation based on multiple samples. The obtained values were subjected to analysis of variance, and the means were separated by Duncan's multiple range test (Super ANOVA, Abacus Concepts, Inc., Berkeley, CA, USA), with $p < 0.05$ considered significant.

## 3. Results and discussion

### 3.1. Mechanism of photochemical ROS generation

Fig. 1 explains the generation of ROS in PVA/AgNPs/BPTA membranes. BPTA can enter a triplet excited state through intersystem crossing (ISC) between systems, which can be directly quenched by oxygen to generate $^1O_2$ or abstract a hydrogen atom from a hydrogen donor to form a quinone group. [8,31]. In the presence of oxygen, quinone groups are quenched to produce ROS [28,32]. However, when a triplet-state quinone group is not fully quenched in the presence of oxygen, competitive reactions such as structural rearrangement and second hydrogen abstraction lead to the formation of a storagly active metastable structure, as exemplified by the light absorption transient structure of membranes [7], which has poor stability and can be easily converted to benzophenone with a concomitant recovery of photosensitive activity [33]. Therefore, PVA/AgNPs/BPTA membranes could readily form and release ROS even in the dark.

### 3.2. Morphology and diameter distribution of the membranes

The surface morphologies, average diameters, and size distributions of the pure PVA and composite membranes were investigated by SEM. Fig. 2 shows SEM images of the PVA membrane, composite membranes with AgNPs, and variable-BPTA-content PVA/AgNPs/BPTA membranes, revealing the presence of Au particles as an artifact of Au sputtering-coating. The average diameter of fibers in the electrospun nanofibrous membrane was calculated by measuring the diameters of 100 randomly selected fibers using ImageJ software. As shown in Fig. 2, the PVA membrane featured a highly uniform and smooth structure with an average diameter of 213.18 ± 64.13 nm. However, the fibers became thicker and more adhesive with an increase in the BPTA content, which was indicative of fiber agglutination and expansion. According to the previous studies, BPTA content increase had no significant effect on the TS ($p > 0.05$) [12]; however, it could result in thick membranes. To observe AgNPs in the fiber membrane, we selected the PVA/AgNPs/BPTA composite membrane prepared at a BPTA concentration of 10 g $L^{-1}$ and featuring hybrid fibers with an average diameter of 240.30 ± 89.59 nm and 1 wt% AgNPs. Fig. 2 shows that the incorporation of 1 wt% AgNPs reduced the average nanofiber diameter by 20 nm (with other electrospinning conditions being the same). Notably, during the electrospinning of the highly conductive solution, the high charge density formed on the surface of the ejected jet made it experience a high extension force [34]. Once charge repulsion overcomes surface tension, the liquid stretches from the "Taylor cone" to form fibers. The addition of AgNPs led to an increase in net charge, and enhanced electrostatic stress caused droplets to rapidly stretch into nanofibers with a smaller diameter [35]. Therefore, fibers in the PVA/AgNPs/BPTA membranes were slightly thinner than those obtained in the absence of AgNPs.

To further probe the incorporation and distribution of AgNPs in the PVA matrix, we probed PVA/AgNPs/BPTA membranes by the energy dispersive analysis of EDAX. During the transfer process, the atoms of each element emit X-rays with unique amounts of energy and the energy of the emitted X-rays can be used to identify the element. The survey X-ray photoelectron spectrum of these fibers confirmed the presence of C, O, and Ag, which is in agreement with the corresponding EDS spectrum (Fig. 3). The existence of the characteristic peak of Ag demonstrated that AgNPs were successfully incorporated into membranes. The quantitative results of the survey spectrum (16.42 wt% Ag, 20.75 wt% O and 62.83 wt% C) clearly confirmed the presence of Ag, O, and C in the structure of the sample. The SEM-EDX elemental mapping of the sample indicated a roughly uniform distribution of the AgNPs inside the polymer matrix.

### 3.3. XRD analysis

The crystallinities of pure PVA and composite membranes were probed by XRD, with patterns of pure PVA, BPTA, PVA/BPTA membranes, AgNPs, and PVA/AgNPs/BPTA membranes shown in Fig. 4. The spectrum of PVA, a typical semi-crystalline polymer, featured a strong peak at $2\theta = 19.8°$ due to PVA inter- and intrachain hydrogen bonding [36]. In the case of AgNPs, peaks at $2\theta = 38.66°$, 44.42°, 64.22°, and 77.16° were ascribed to reflections from (111), (200), (220), (311), and (222) planes, respectively [5]. Fig. 4 shows a wide-scan pattern of pristine AgNPs, revealing that the observed peaks can be assigned to face-centered-cubic Ag with a strongly preferred (111) orientation, in line with JCPDS 4–0783 [37]. The pattern of the PVA/AgNPs/BPTA membrane showed characteristic peaks of the three components. As PVA crystallization was inhibited through intermolecular complexation with BPTA (which formed new hydrogen bonds with PVA chains at the expense of existing intra- and interchain hydrogen bonds), the PVA/AgNPs/BPTA composite peak at ~ 19.8° was weaker and narrower than that of pure PVA. The patterns of PVA/AgNPs and PVA/AgNPs/BPTA membranes confirmed the presence of AgNPs, and the structure of

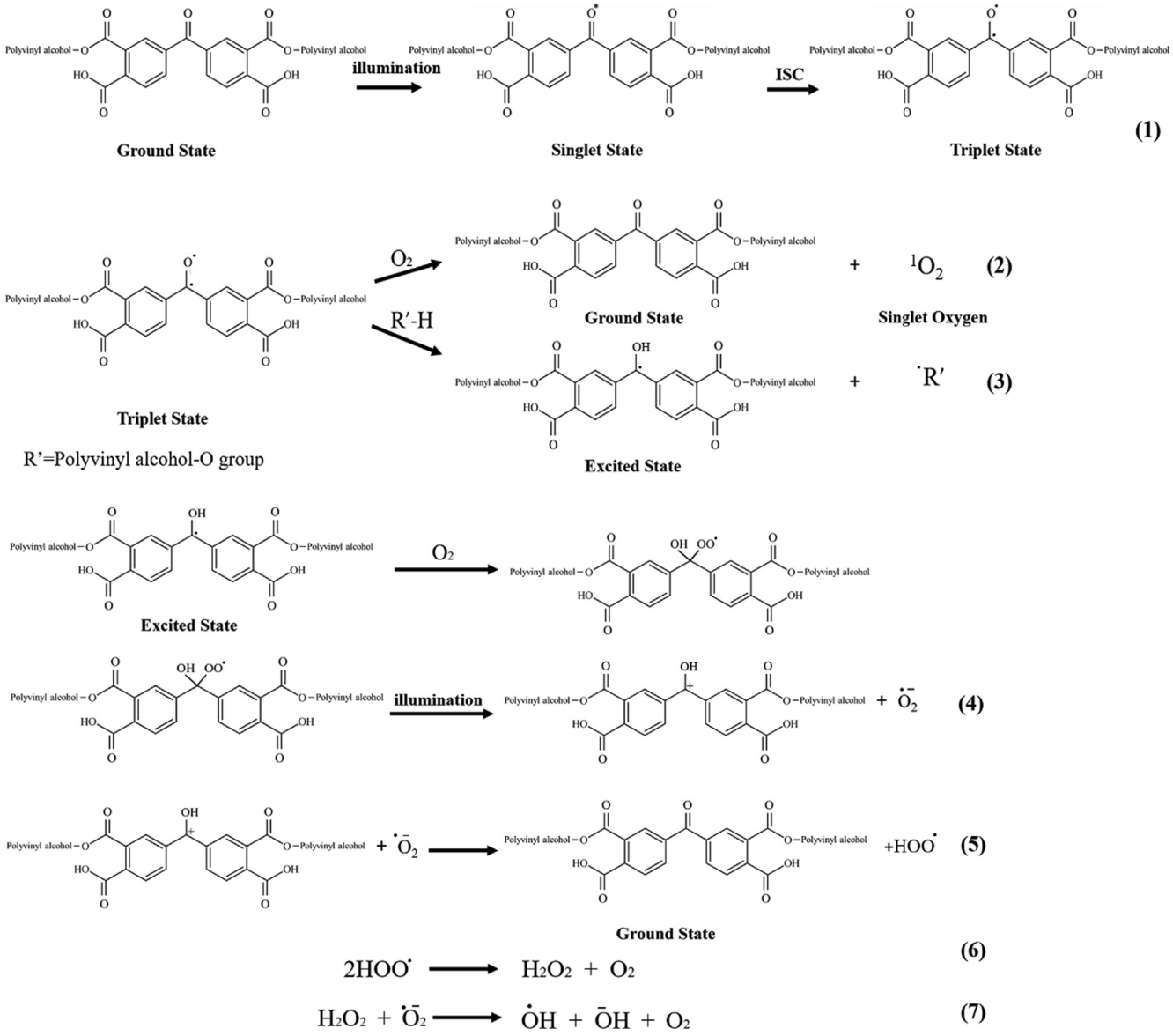


**Fig. 1.** Synthesis of photoinduced ROS generation.

incorporated BPTA was further probed by FTIR-ATR spectroscopy.

### 3.4. FTIR spectroscopy analysis

Fig. 5 shows the chemical structure of pure PVA, PVA/AgNPs/BPTA composite membranes, and the corresponding FTIR-ATR spectra. The spectrum of PVA featured characteristics peaks at 3293, 2924, 1327, and 1093 $cm^{-1}$ representing −OH stretching, C−H stretching, C−H bending, and C−O stretching, respectively [38]. The asymmetric and symmetric vibration peaks of BPTA carboxyl groups were located at 1621 and 1440 $cm^{-1}$, respectively, whereas the COOH peak of pure BPTA was observed at 1700 $cm^{-1}$. In the spectra of BPTA-grafted composite membranes, peaks at 1586 and 1230 $cm^{-1}$ were attributed to ester O−C═O and C−O moieties, respectively [39]. The spectra of BPTA-containing composite membranes featured a new ester peak at 1722 $cm^{-1}$, indicating the successful incorporation of BPTCD [40]. The similarity of the neat PVA and PVA/AgNPs composite membrane spectra suggested that the chemical structure of PVA did not change after AgNPs incorporation. However, the peak at 3330 $cm^{-1}$ gained intensity after composite membrane formation, which indicated that BPTA and AgNPs engaged in hydrogen bonding with PVA. The effects of AgNPs on PVA composites and other polymer systems have also been described by other authors. This behavior indicated that the cross-linking of PVA chains was affected by the above PVA-AgNPs hydrogen bonding [41]. In addition, in the presence of AgNPs, the band at 1374 $cm^{-1}$ shifted to higher wavenumbers because of the intensified interaction between PVA–OH groups and AgNPs. This interaction limited the outer curved plane and PVA–OH group oscillation, which, in turn, affected PVA chain mobility and physical cross-linking [42].

### 3.5. DSC measurements

The heat resistance and thermal stability of composite membranes containing BPTA and AgNPs were probed by DSC in an atmosphere of $N_2$. Fig. 6 displays DSC thermograms of pure PVA as well as PVA/AgNPs, and PVA/AgNPs/BPTA blends, which were recorded within a temperature range of 50–350 °C. The thermogram of catalyst-free BPTA featured an endothermic peak at 223 °C. The exothermic peak of pure BPTA was sharper than that of the composite membrane, which was ascribed to the lower crystallization time due to the increased crystallization rate. The intensity of the (weak) melting peak of neat PVA at 220 °C was related to the PVA crystallinity degree. However, the

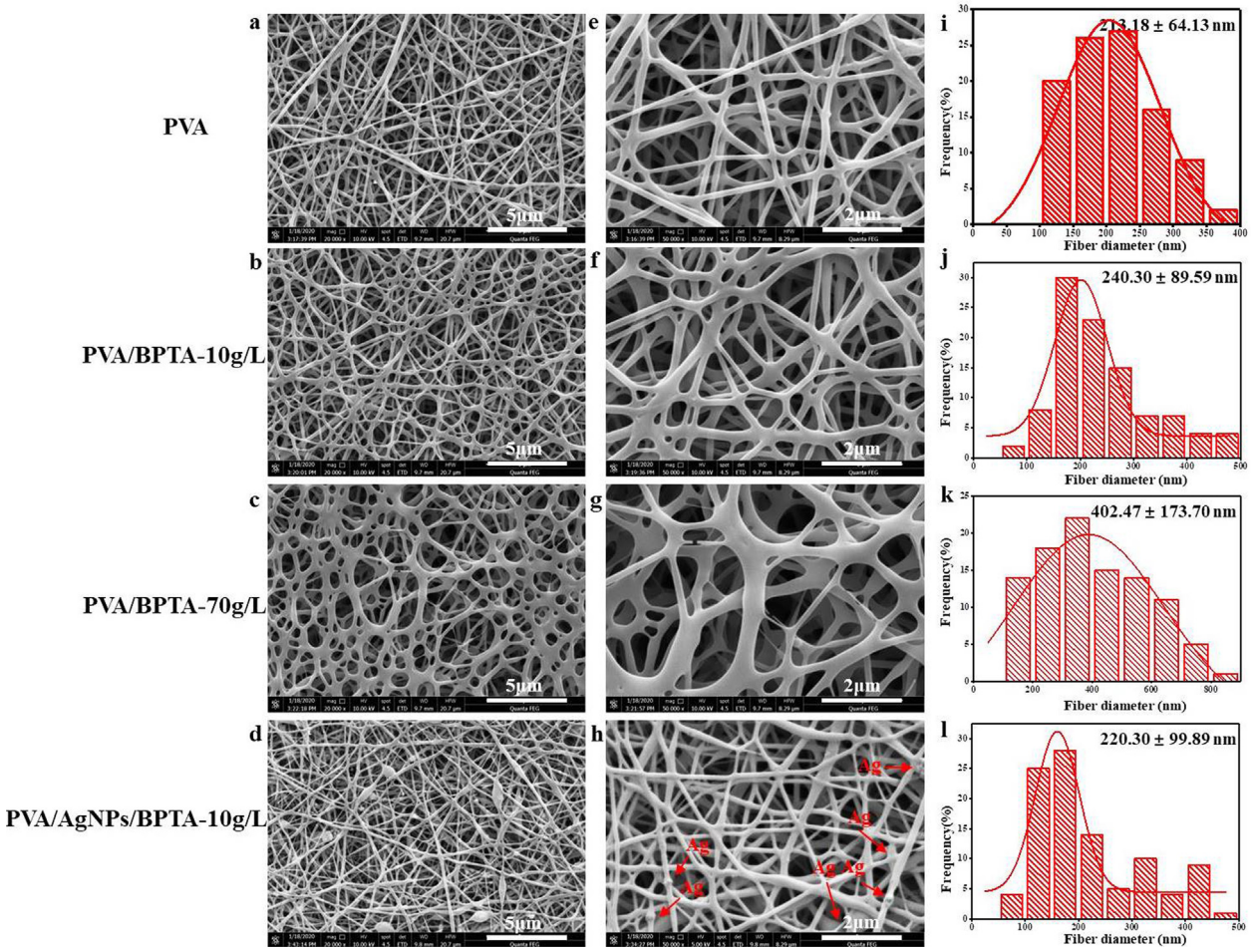


**Fig. 2.** (a-d) SEM images of electrospun membranes; (e-h) magnified images of electrospun nanofibers; (i-l) diameter of nanofibers determined from SEM images using ImageJ software.

incorporation of AgNPs into the composite membrane resulted in the dominance of an exothermic peak in the same temperature range. In BPTA-containing composite membranes, the PVA melting peak was covered by this strong exothermic peak, attributed to the reaction of BPTA with the molten polymer matrix. The incorporation of BPTA and AgNPs resulted in a shift of the endothermic peak from 222.9 to 199.1 °C and made it wider and less intense, indicating hindered crystallization. These phenomena indicated the occurrence of thermal induction resulting in the reduction of Ag, mainly due to the presence of organic components or possible crystallization of amorphous AgNPs formed during membrane preparation [19]. An additional endothermic peak of PVA starting at 85 °C and the glass transition temperature (Tg) of the PVA film were related. Our FTIR spectral analysis proved that Ag and PVA in the composite film were not chemically bonded. Therefore, the weak change in PVA/AgNPs is mainly due to the crystallization of the composite material itself. However, the Tg of PVA/BPTA is higher than that of PVA, because a large amount of cross-linking generally increases the Tg [43].

### 3.6. Mechanical properties

Although numerous synthetic- and natural-polymer-based materials exhibit excellent antibacterial activity, their applicability is limited by poor mechanical properties [44]. To mitigate this problem, PVA-Ag nanofibrous membranes have been developed and applied in many fields, as exemplified by the high-mechanical-strength composites described herein. The effects of incorporating AgNPs and BPTA into nanofibrous membranes on the elastoplastic response of these membranes were studied by tensile testing (Fig. 7). Compared with the pure PVA membrane, the composite membranes had significantly higher EB and TS ($p < 0.05$), which demonstrated the effectiveness of PVA supplementation with AgNPs at low loadings, in line with the results of Fortunati et al [41]. The increase in mechanical strength was attributed to the physical interaction between the polymer matrix and AgNPs, i.e., to the distribution of AgNPs within the polymer matrix to form a large interfacial contact area. The introduction of AgNPs also increased the crystallinity of the PVA/BPTA matrix and the fracture stress of the corresponding membranes [4]. Thus, AgNPs were concluded to significantly enhance the mechanical properties of nanofibrous membranes. With the increasing BPTA content, the EB of the PVA/AgNPs/BPTA composite membrane first increased and then decreased, while the TS remained stable. These changes were ascribed to the microscale network structure and intermolecular forces generated in the membrane matrix because of organic matter cross-linking. The TS of cross-linked composite membranes increased because of the addition of BPTA to fibers and the TS reached the maximum with BPTA content up to 30 g/L. This finding reveals that chemical modification provided a large interfacial contact area, which improved the interfacial adhesion between the grafted BPTA and the matrix [45]. In line with SEM observations, an increase in BPTA content from 50 to 70 g $L^{-1}$ resulted in a decrease in EB owing to the reduced magnitude of attractive forces between matrix chains [46]. This finding can be attributed to the surface modification of the film, which improved the adhesion between the blend layers and the surface of BPTA, thereby mechanically anchoring the film on the structure when grafting with a high concentration of BPTA [45].

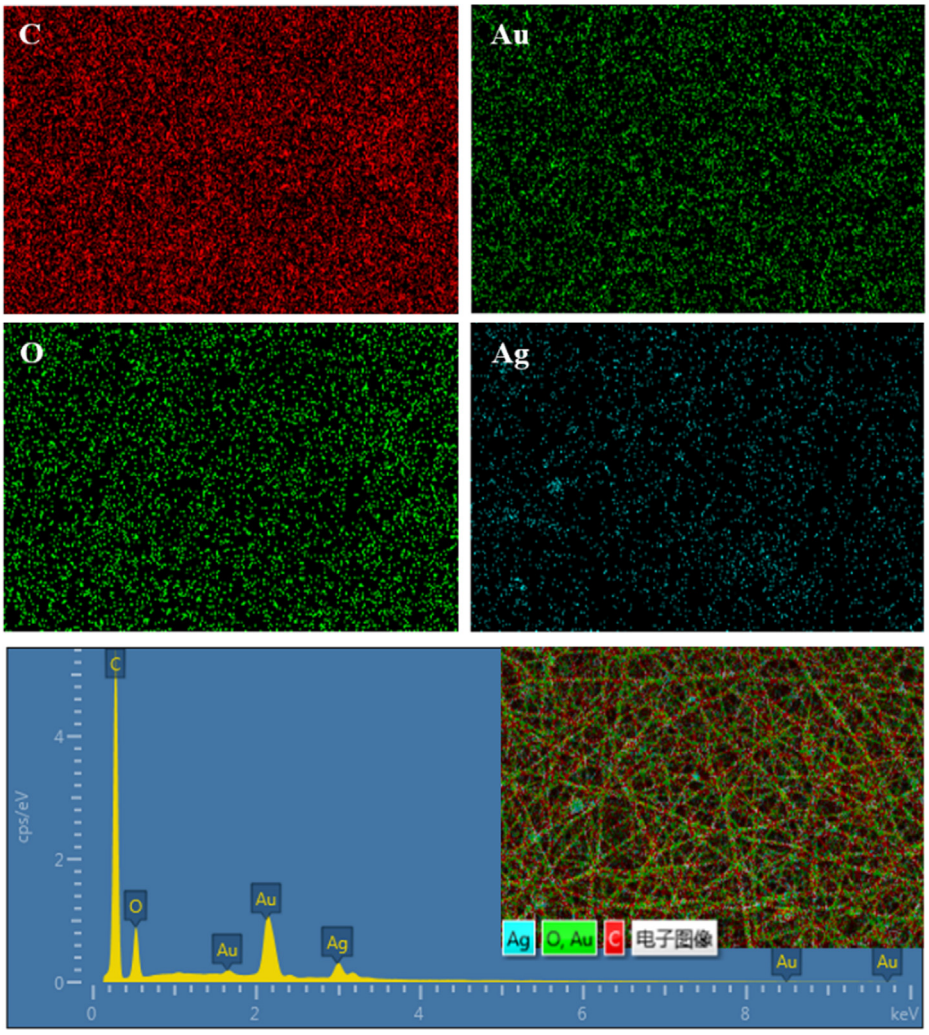


**Fig. 3.** Elemental mapping images of PVA/AgNPs/BPTA membranes, and the elemental distributions of C, Au, O and Ag.

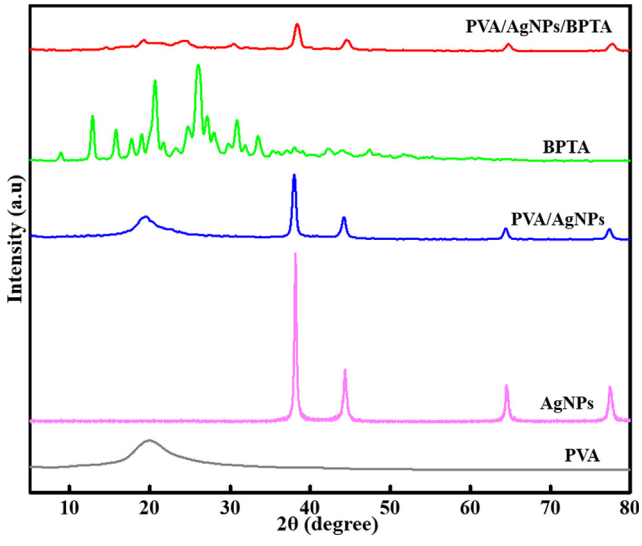


**Fig. 4.** XRD patterns of BPTA, AgNPs, PVA, and composite membranes.

### 3.7. Analysis of ROS production

To quantify ROS rechargeability, we first exposed variable-BPTA-content PVA/AgNPs/BPTA membranes to 1-h daylight irradiation and measured OH· production every 10 min, revealing that > 90% of ROS was rapidly released in the first 10 min, and the amounts of OH· and $H_2O_2$ subsequently reached equilibrium (Fig. 8 (a) and (b)), which is in line with the results reported by Yi et al [33]. PVA and PVA/AgNPs membranes with the same BPTA content showed similar ROS production profiles, which suggested that AgNPs do not directly generate ROS or hinder their formation. Banerje et al. observed the bactericidal effect of AgNPs-containing nanocomposites due to ROS-generated oxidative stress in the cytoplasm of bacterial cells [6]. As expected, PVA/AgNPs/BPTA membranes featured the highest charging capacity. ROS production increased with an increase in the BPTA content, reaching saturation at a BPTA concentration of 50 g $L^{-1}$. The number of produced OH· radicals was determined by the number of benzophenone moieties on the membrane, which also saturated at a BPTA level of 50 g $L^{-1}$. After 1 h of daytime charging, the release of OH· and $H_2O_2$ was 7378.601 and 622.55 μg $g^{-1}$, respectively, corresponding to charging rates of 130.63 and 10.38 μg $g^{-1}$ $min^{-1}$, respectively, and indicating the utilization of large amounts of light energy. A cyclic irradiation test with a 30-min-interval light–dark fatigue cycle performed on PVA grafted with BPTA at 50 g $L^{-1}$ (Fig. 8(c) and (d)) showed that OH· and $H_2O_2$ production was mainly observed during the irradiation period and ceased in the dark. The amount of ROS steadily increased after irradiation, although activity did not significantly decrease ($p > 0.05$), which is in agreement with previously reported results [7].

Subsequently, we explored the reusability of composite membranes to evaluate the economic viability of their practical application. The

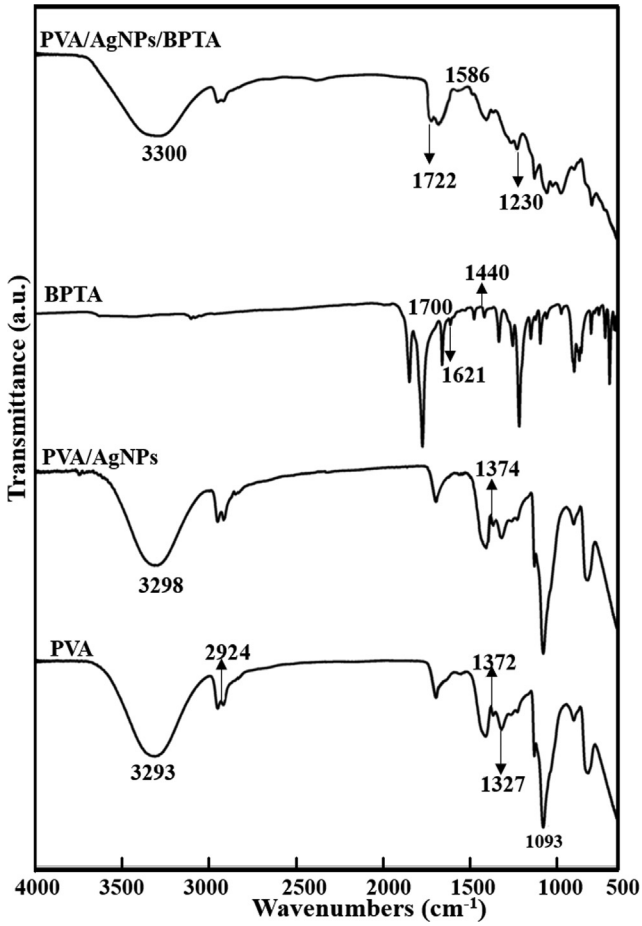


**Fig. 5.** FTIR analysis of PVA/AgNPs/BPTA, PVA/AgNPs, PVA, and BPTA.

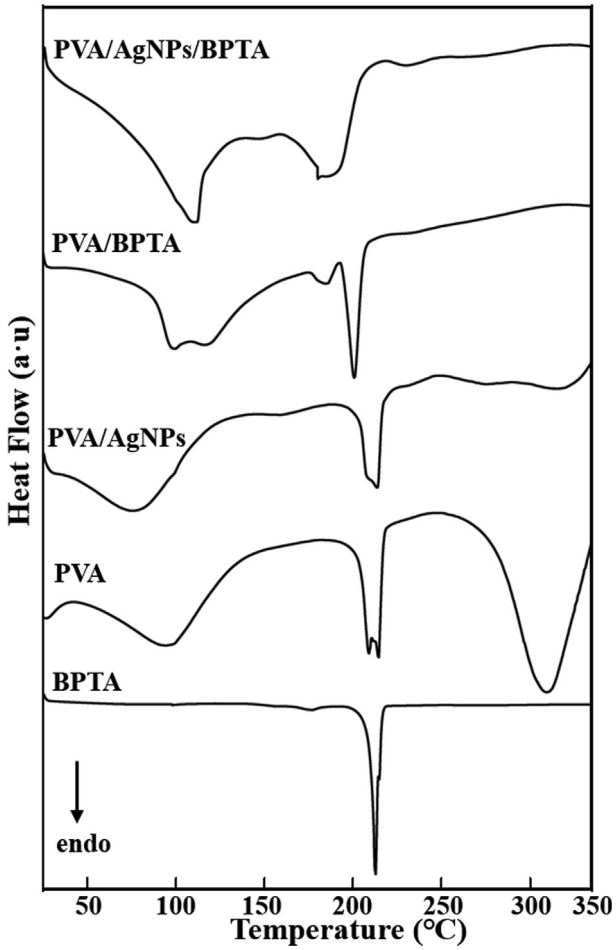


**Fig. 6.** DSC curves of BPTA, PVA, and different composite membranes.

recharging cycle test of PVA/AgNPs/50-g $L^{-1}$ BPTA composite membranes was performed as displayed in Fig. 8(e). In each cycle, the membranes were first irradiated for 1 h and then completely quenched with excess thiosulfate solution. After seven cycles, no significant reduction of recharging capacity was observed, i.e., the composite membrane retained 72.5 and 76.3% of its original OH· and $H_2O_2$ charging capacities, respectively. This behavior highlights the structural stability of the tested membrane, showing that it can be employed as a multiple-use medical protective material.

### 3.8. Antibacterial activity

Antibacterial activity is another basic requirement for PPE materials intended for medical use, especially in the case of the increasingly serious virus outbreaks currently facing the public. The antibacterial activity of membranes was described by the size of the corresponding inhibition region for Gram-positive *S. aureus* and Gram-negative *E. coli*, as shown in Fig. 9. The PVA membrane exhibited no inhibitory effect on both bacteria, while the PVA/AgNPs/BPTA membranes showed significant *S. aureus* inhibition zones with diameters (9.14–18.2 mm) positively correlated with BPTA content (Table 1). This bactericidal effect was ascribed to the breakdown of the bacterial cytoplasmic membrane/cell wall and the leakage of pathogens into the cytoplasm [47]. However, the activity of such membranes against *S. aureus* has been reported to be stronger than that against *E. coli* [48]. The cell wall structures of Gram-positive and -negative microorganisms are different, with those of the latter featuring a polysaccharide membrane thicker than the peptidoglycan membrane of the former, which makes the structure and chemistry of Gram-negative bacteria more complex. Henece, PVA/AgNPs/BPTA membranes exhibit higher antibacterial actibity against these bacteria [49].

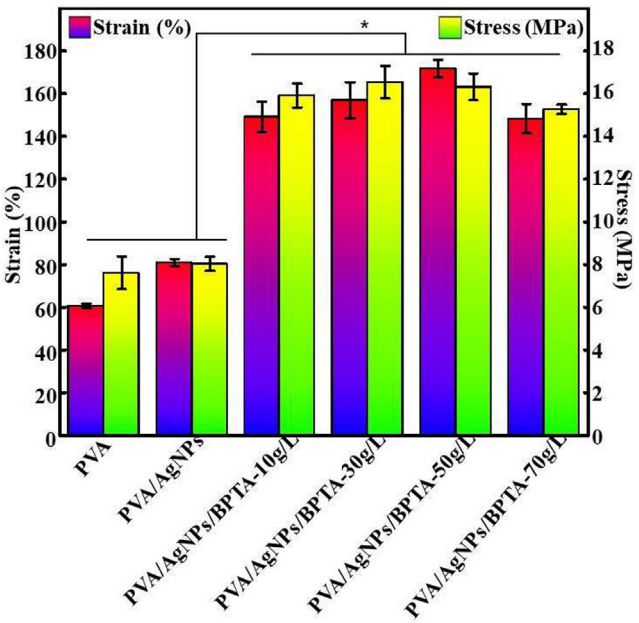


**Fig. 7.** Mechanical properties of different composite membranes.

The small grain size and large specific surface area of nanocomposites may benefit antibacterial activity [37], although the exact mechanism of the antibacterial action of AgNPs remains controversial.

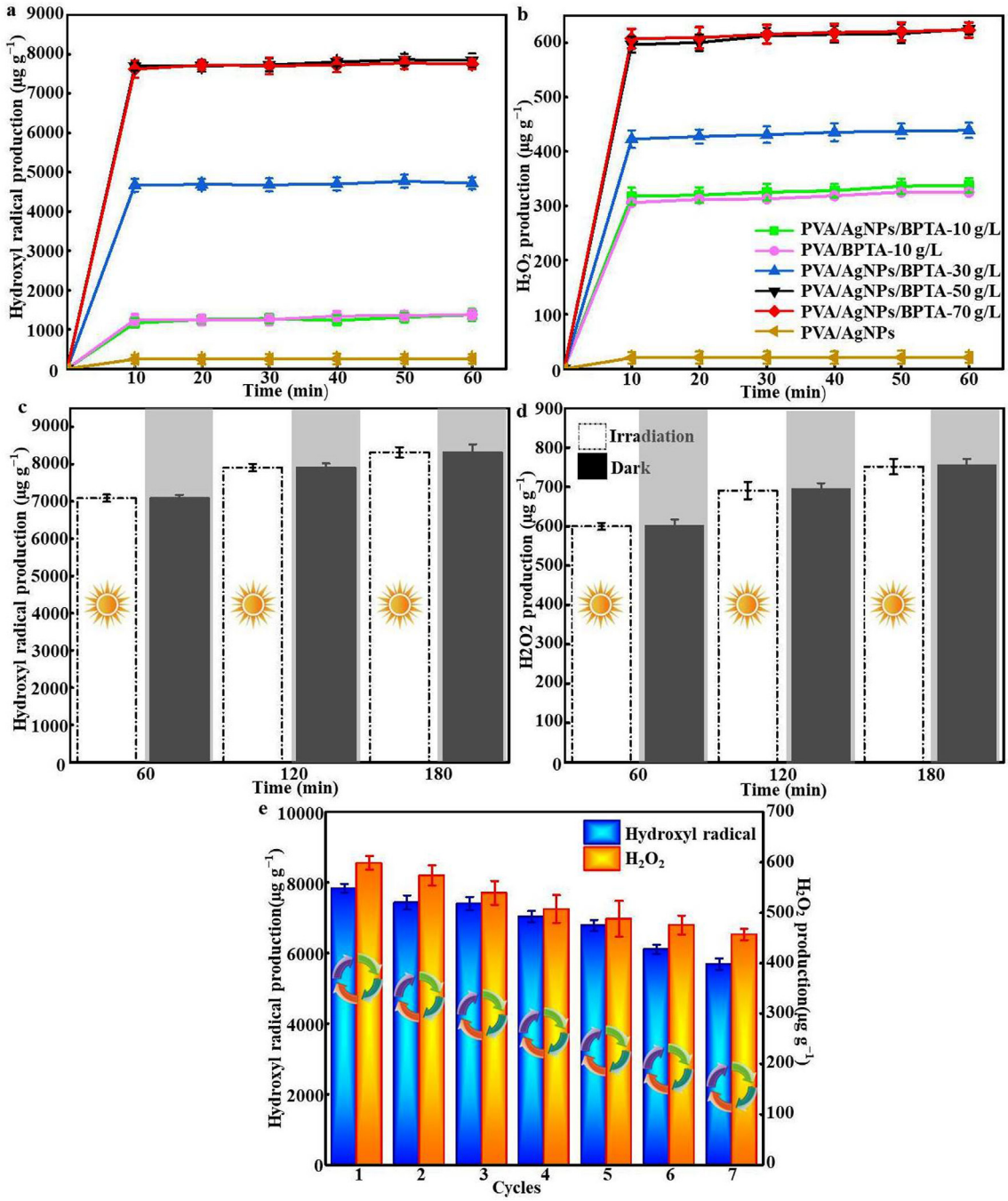


**Fig. 8.** (a, b) Amounts of OH· and $H_2O_2$ produced by samples over 60 min; (c, d) Time course of OH· and $H_2O_2$ production over PVA/AgNPs/50-g $L^{-1}$ BPTA (irradiation period = white, dark period = gray); (e) Evaluation of PVA/AgNPs/50-g $L^{-1}$ BPTA rechargeability by repeated charging and quenching over seven cycles.

According to the results of ROS production analysis, the presence of AgNPs did not significantly impact the amount of active oxygen produced by membranes. This finding further proves that AgNPs can promote the production of ROS by cells and anchor to the bacterial cell wall to produce "pits" on their surface and subsequently make their way into cells to induce structural changes of the cell membrane and eventually cell death [50]. Therefore, even though the corresponding ROS production profiles were not significantly different ($p > 0.05$), the inhibition zone of PVA/Ag/50-g $L^{-1}$ BPTA was larger than that of PVA/50-g $L^{-1}$ BPTA for both *E. coli* and *S. aureus*, which indicated the existence of a synergistic effect of AgNPs and BPTA on antibacterial ability.

### 3.9. Color and light transmission

The color values (L*, a*, and b*) and total color differences (ΔE*) of pure PVA and composite membranes are listed in Table 2. L*, a*, and b* values provide an objective evaluation of the composite membrane appearance, whereas ΔE* reflects the treatment-induced color change relative to the reference color [51]. L*, which represents lightness, decreased upon the incorporation of AgNPs and BPTA ($p < 0.05$), i.e., the membrane color concomitantly changed to a darker hue. The values of a*, reflecting green–red color prevalence, were negative for all membranes except for pure PVA, i.e., composite membranes were not truly red. The values of b*, reflecting blue-yellow color prevalence,

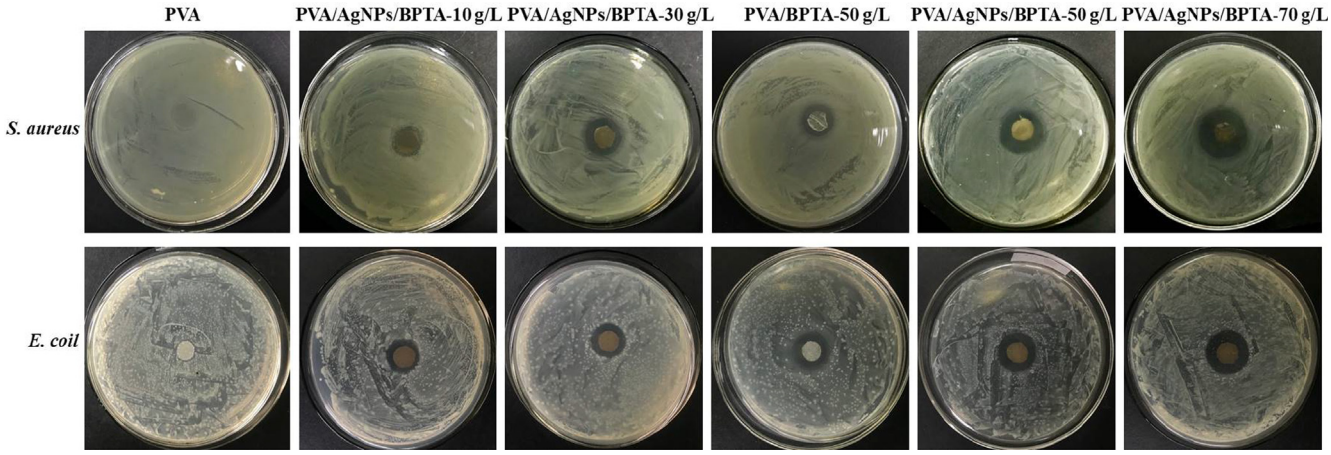


**Fig. 9.** Inhibition zones of PVA with different BPTA contents against *S. aureus* and *E. coli*.

**Table 1**
Antimicrobial properties of PVA/AgNPs membranes without and with BPTA.

| Samples | Diameter of inhibition zone (mm) | |
|---|---|---|
| | *S. aureus* | *E. coli* |
| PVA | ND | ND |
| PVA/AgNPs/BPTA-10 g/L | 9.11 ± 0.03$^{e}$ | 11.54 ± 0.14$^{d}$ |
| PVA/AgNPs/BPTA-30 g/L | 13.43 ± 0.11$^{d}$ | 13.41 ± 0.37$^{c}$ |
| PVA/BPTA-50 g/L | 14.81 ± 0.06$^{c}$ | 14.12 ± 0.14$^{c}$ |
| PVA/AgNPs/BPTA-50 g/L | 15.94 ± 0.10$^{b}$ | 15.55 ± 0.29$^{b}$ |
| PVA/AgNPs/BPTA-70 g/L | 18.12 ± 0.08$^{a}$ | 16.41 ± 0.05$^{a}$ |

Values are presented as mean ± standard deviation. Different letters in the same column indicate significant differences ($p < 0.05$).

increased upon the incorporation of AgNPs and BPTA ($p < 0.05$), indicating a slight increase in yellowness. The highest b* value of 7.21 was observed for PVA/Ag/30-g $L^{-1}$ BPTA, which is in agreement with the corresponding value of a*, indicating the presence of colored compounds in composite membranes [52]. In addition, ΔE* showed a trend similar to that of b* except for pure PVA as the control group and ranged from 48.07 to 23.79, which indicated that the absolute color difference could be easily detected by the human eye ($p < 0.05$) [53].

### 3.10. MC and SD

Table 2 shows that with the increasing BPTA content, MC first increased and then decreased. At BPTA concentrations above 50 g $L^{-1}$, excess BPTA easily precipitated and crystallized to reduce the compactness of the composite membranes and afford pore defects, which, in turn, decreased MC. Meanwhile, the insignificant increase in MC ($p > 0.05$) upon incorporating AgNPs into pure PVA was associated with the structural differences of the polymer matrix, specifically with the dependence of chain arrangement on the initial ionic strength of the aqueous medium and the molecular interactions with Ag species in this medium. At a low AgNPs loading, macromolecular chains were extended via linkage with Ag species, which increased the tortuous coefficient of water molecule diffusion [54].

Water absorption is an important indicator of material water resistance. Herein, to eliminate the effects of the differences in the initial membrane weights, we quantified the water absorption of different membranes over 24 h (Table 2), revealing that pure PVA easily absorbed water to achieve a water absorption efficiency of > 38%. After blending with BPTA, the water absorption efficiency of composite membranes decreased. The water absorption efficiency of the PVA/AgNPs/BPTA composite membrane was significantly lower than that of pure PVA ($p < 0.05$), while that of the PVA/AgNPs membrane was not significantly different ($p > 0.05$). This behavior was ascribed to the fact that although the content of AgNPs was low, these NPs formed a three-dimensional structure when mixed with BPTA. Upon intercalation, PVA chains experienced stronger intermolecular forces than a single two-dimensional structure and therefore did not readily combine with water molecules.

### 3.11. WVP

The WVP values revealed that water molecules and the polymer matrix engaged in interactions that could promote the adsorption and diffusion of influent molecules and thus hinder desorption [55]. The permeability of the PVA composite membrane was generally lower than that of the corresponding cast membranes, as the tightly connected three-dimensional network of the former hinders the migration of water vapor through nanofibers ($p < 0.05$) [56]. Table 2 lists the WVPs of the composite membranes, showing that at a constant BPTA content, the WVP of the PVA and PVA/AgNPs membranes decreased upon AgNPs incorporation, in line with the results of Sarwar et al [4]. This behavior was ascribed to the strengthening of interactions between polymer chains after AgNPs incorporation and the concomitant decrease in internal intermolecular distance and free volume. The formation of a composite membrane with a tight and more complex network structure increased the diffusion path length of water vapor and

**Table 2**
L*, a*, b*, ΔE, moisture content (MC), swelling degree (SD), and water vapor permeability (WVP) of different nanocomposite films.

| Samples | L* | a* | b* | ΔE | MC % | SD % | WVP × $10^{-11}$ (g·$Pa^{-1}s^{-1}m^{-1}$) |
|---|---|---|---|---|---|---|---|
| PVA | 96.49 ± 0.23$^{a}$ | 6.49 ± 0.18$^{a}$ | 3.61 ± 0.08$^{c}$ | 9.91 ± 0.29$^{c}$ | 8.30 ± 0.09$^{d}$ | 37.14 ± 2.56$^{a}$ | 20.72 ± 0.32$^{a}$ |
| PVA/AgNPs | 66.77 ± 0.43$^{b}$ | 5.11 ± 0.10$^{b}$ | 3.77 ± 0.40$^{b}$ | 23.79 ± 0.39$^{b}$ | 9.81 ± 1.16$^{cd}$ | 38.46 ± 1.71$^{a}$ | 14.81 ± 0.42$^{b}$ |
| PVA/AgNPs/BPTA-10 g/L | 42.05 ± 0.45$^{c}$ | 1.70 ± 0.24$^{c}$ | 7.20 ± 0.28$^{a}$ | 48.07 ± 0.46$^{a}$ | 11.79 ± 0.39$^{bc}$ | 35.81 ± 0.61$^{a}$ | 10.51 ± 0.09$^{c}$ |
| PVA/AgNPs/BPTA-30 g/L | 42.08 ± 0.47$^{c}$ | 1.83 ± 0.22$^{c}$ | 7.21 ± 0.08$^{a}$ | 48.05 ± 0.47$^{a}$ | 13.37 ± 0.67$^{ab}$ | 34.66 ± 1.01$^{a}$ | 9.08 ± 0.16$^{d}$ |
| PVA/AgNPs/BPTA-50 g/L | 42.11 ± 0.49$^{c}$ | 1.84 ± 0.22$^{c}$ | 7.21 ± 0.07$^{a}$ | 48.01 ± 0.48$^{a}$ | 14.94 ± 0.43$^{a}$ | 33.22 ± 2.72$^{ab}$ | 6.05 ± 0.08$^{e}$ |
| PVA/AgNPs/BPTA-70 g/L | 42.32 ± 0.22$^{c}$ | 1.82 ± 0.37$^{c}$ | 7.19 ± 0.13$^{a}$ | 47.80 ± 0.21$^{a}$ | 13.44 ± 0.17$^{ab}$ | 27.73 ± 0.99$^{b}$ | 10.81 ± 0.22$^{c}$ |

Values are presented as mean ± standard deviation. Different letters in the same column indicate significant differences ($p < 0.05$).

thus reduced the diffusion and solubility coefficients [57]. The WVP of the PVA/AgNPs/BPTA membrane decreased with the increasing BPTA content and was lower than that of the PVA/AgNPs membrane, which was ascribed to a concomitant decrease in membrane hydrophilicity due to ester bond formation upon BPTA grafting. However, WVP did not always decrease with the increasing BPTA content, as overly high BPTA loadings resulted in a damaged internal structure of fibers and, hence, in increased WVP, which was, nevertheless, still lower than that of the pure PVA membrane.

### 3.12. Antioxidant activity

The antioxidant defense system works by blocking the production of free radicals, scavenging oxidants, preventing the chain growth of these oxidants, and improving the endogenous antioxidant activity of involved substances. These defense tools work together to defend the body from oxidative stress [58]. DPPH is a nitrogen-centered free radical often used to estimate the radical scavenging activity of antioxidants. In the presence of antioxidants, DPPH is quenched to afford yellow diphenyl pyridinomethyl hydrazine, and the accompanying absorbance decrease is used as a measure of antioxidant hydrogen bonding ability [59]. In general, DPPH clearance efficiency is positively correlated with antioxidant capacity ($p < 0.05$). According to previous studies, Ag loadings of $< 0.02$ wt% can result in DPPH clearance efficiencies of $> 20\%$ [60]. Herein, clearance efficiencies of $> 60\%$ were achieved for membranes with 1 wt% AgNPs (Fig. 10). Nakkala et al. showed that AgNPs can gain or lose electrons to form stable species and thus effectively quench free radicals [61]. Hence, the PVA/AgNPs/BPTA composite membrane supplemented with AgNPs may act as antioxidants owing to the presence of proton-donating (amino and hydroxyl) groups. DPPH scavenging activity slowly increased with the increasing BPTA content; therefore, the antioxidant activity of the composite membranes was concluded to mainly depend on the addition of AgNPs.

### 3.13. Filtration performance evaluation and bioprotection application

The ability of the fibrous membrane to intercept ultrafine particles was studied, and the filtration performance was evaluated using polydisperse NaCl particles with diameters of 300 to 500 nm under increasing airflow. As shown in Fig. 11(a), as the gas flow increases, the filtration efficiency of PVA/AgNPs/BPTA-50 g $L^{-1}$ sample decreases. The lower the gas flow rate, the more sufficient are collisions between NaCl particles and fibers under the diffusion effect, resulting in a higher filtration capacity. As the airflow rate increased from 10 to 90 L $min^{-1}$, the filtration efficiency of the membrane decreased from 99.98 to 98.54%, which was still significantly higher than that of the N95 mask (95%), reflecting the excellent filtration performance of the sample [11]. The membranes with PVA as the base material are relatively dense, and the pressure drop in the mask material is large. During experiments, the pressure drop increased linearly with the increasing air flow velocity. Compared with the N95 mask, the nanofiber structure of the sample had worse permeability. The SEM results in Fig. 11(b) show that many aerosol particles were intercepted on the top surface of the membrane under air flow at 90 L $min^{-1}$ for 5 min. At the same time, the filtered membrane still maintained its integrated structure. The pressure drop is directly related to the basis weight of the membrane. Some commercial filters have a filtration efficiency of 98.09% for 300–500-nm particles, accompanied by a pressure drop of 188 Pa. As shown in Fig. 11 (c), as the basis weight of the membranes increased from 2.1 g $m^{-2}$ to 14.9 g $m^{-2}$, the pressure drop showed a significant increasing trend, which was proportional to the unit weight of the fibrous membrane. The minimum pressure drop of NaCl with a basis weight of 2.1 g $m^{-2}$ to NaCl was 168 Pa, corresponding to a higher QF value. The higher basis weight resulted in a thicker network structure and increased the flexibility of the airflow channels, providing more contact points between particles and nanofibers [62].

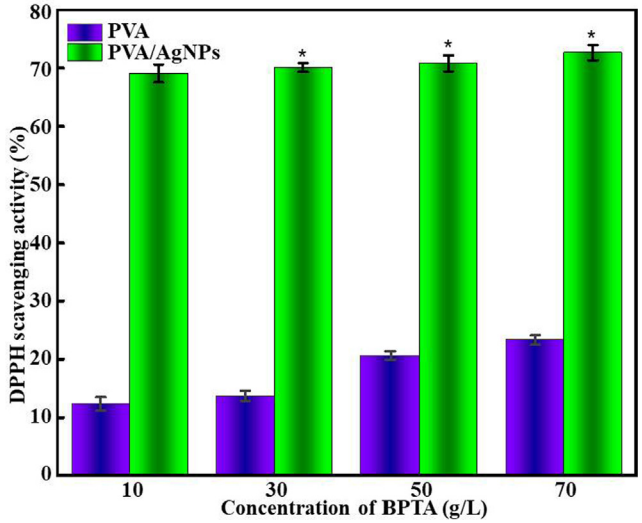


**Fig. 10.** DPPH scavenging activity of composite membranes with and without AgNPs.

As shown in Fig. 11(d), a $1 \times 10^6$ cfu aerosol containing *E. coli* was prepared as a model infection aerosol, the size of which was similar to that of aerosols produced by human sneezing or coughing. PVA/AgNPs/BPTA-50 g $L^{-1}$ was attached to the right side of an N95 mask and irradiated for 1 h for comparison with a dust mask without antibacterial properties. On the control area, *E. coli* showed high activity, with free growth and proliferation. As shown in Fig. 11(e), after four experiments, the antibacterial effect of the N95 area decreased significantly. In contrast, in the experimental sample area, the inhibitory rate was consistently over 90%, indicating strong protection against pathogens and high reusability.

## 4. Conclusions

PVA/AgNPs membranes were prepared by electrospinning and catalytically grafted with BPTA to prepare the PVA/AgNPs/BPTA composite membrane. SEM images showed that AgNPs were uniformly dispersed in the PVA matrix and that fiber diameter increased. Moreover, introducing AgNPs into PVA membranes decreased their WVP and enhanced their mechanical properties. XRD and FTIR spectroscopic analyses confirmed the presence of AgNPs and the formation of ester bonds upon BPTA grafting. The PVA/AgNPs/BPTA composite membrane showed excellent antimicrobial activity. In addition, the PVA/AgNPs/BPTA composite membranes could produce ROS under both light and dark conditions. After the generated ROS were quenched, these membranes were subjected to seven repeated ROS generation cycles, and were shown to retain $> 70\%$ of their original OH· and $H_2O_2$ charging capacity. In the filtration test, the membranes showed high filtration efficiencies of 99.98% for NaCl and held a relatively low pressure drop of 168 Pa with a basis weight of 2.1 g $m^{-2}$. After being sprayed with *E. coli* aerosols seven times, the membranes still had a stronger antibacterial potency than N95 masks, which reflected the reusability of the membranes. Thus, the cross-linked PVA/AgNPs membrane reinforced with grafted BPTA was concluded to be structurally stable and reusable, thus being well suited for use as a medical protective material.

## CRediT authorship contribution statement

**Siying Li:** Resources, Writing - original draft. **Rong Zhang:** Data curation, Writing - review & editing. **Junlan Xie:** Investigation, Data curation. **Dur E. Sameen:** Investigation, Methodology. **Saeed Ahmed:**

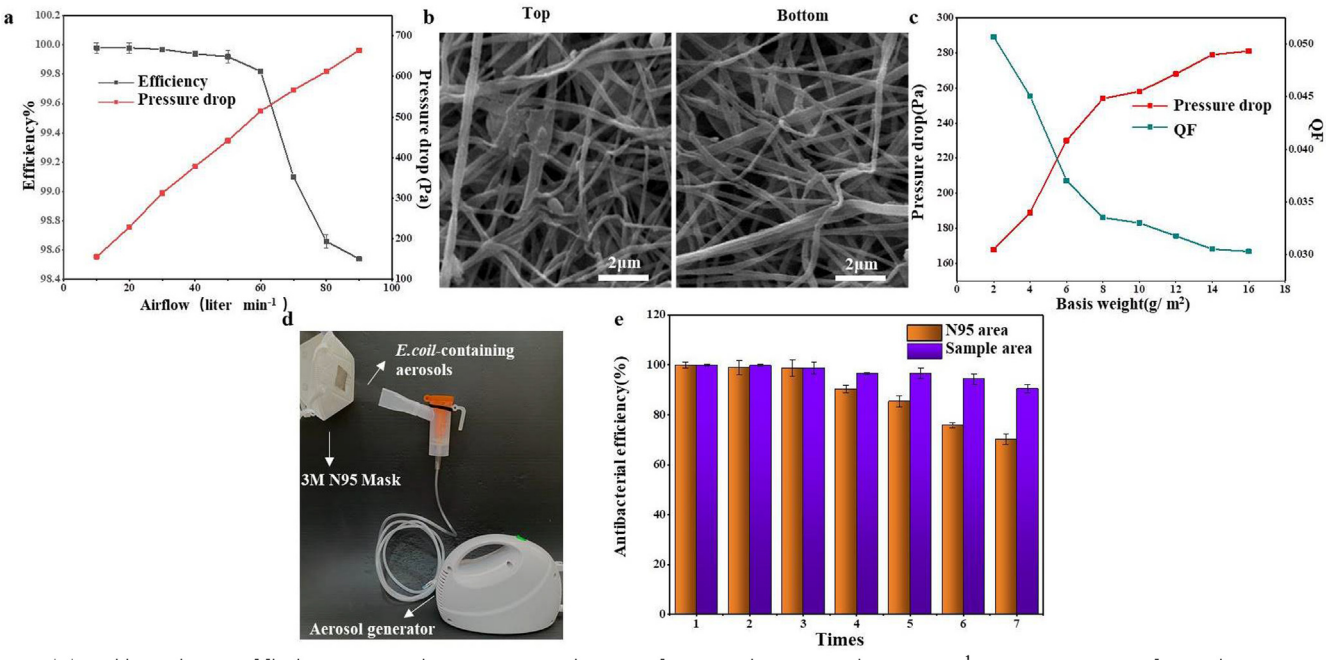


**Fig. 11.** (a) Filtration efficiency and pressure drop of PVA/AgNPs/50-g $L^{-1}$ BPTA as a function of airflow;(b) SEM images of the top and bottom surface of PVA/AgNPs/50-g $L^{-1}$ after filtration; (c) QF values and pressure drop of PVA/AgNPs/50-g $L^{-1}$ with various basis weights; (d) bacterial-aerosol-generating device and N95 mask intercept test; (e) comparison of the antibacterial rates of an N95 mask and PVA/AgNPs/50-g $L^{-1}$ over seven interception cycles.

Formal analysis. **Jianwu Dai:** Software. **Wen Qin:** Visualization. **Suqing Li:** Validation. **Yaowen Liu:** Conceptualization, Supervision.

## Declaration of Competing Interest

The authors declare that they have no known competing financial interests or personal relationships that could have appeared to influence the work reported in this paper.

## Acknowledgments

This work was supported by National Natural Science Foundation of China (51703147), National Fund of China Scholarship Council (201806915013), Sichuan Science and Technology Program (2018RZ0034), and Natural Science Fund of Education Department of Sichuan Province (16ZB0044 and 035Z1373).

## References

[1] C. Wang, P.W. Horby, F.G. Hayden, G.F. Gao, A novel coronavirus outbreak of global health concern, The Lancet 395 (2020) 470–473, https://doi.org/10.1016/s0140-6736(20)30185-9.
[2] M. Zhu, R. Xiong, C. Huang, Bio-based and photocrosslinked electrospun antibacterial nanofibrous membranes for air filtration, Carbohydr. Polym. 205 (2019) 55–62, https://doi.org/10.1016/j.carbpol.2018.09.075.
[3] C. Isik, G. Arabaci, Y. Ispirli Dogac, I. Deveci, M. Teke, Synthesis and characterization of electrospun PVA/Zn(2+) metal composite nanofibers for lipase immobilization with effective thermal, pH stabilities and reusability, Mater. Sci. Eng. C Mater. Biol. Appl. 99 (2019) 1226–1235, https://doi.org/10.1016/j.msec.2019.02.031.
[4] M.S. Sarwar, M.B.K. Niazi, Z. Jahan, T. Ahmad, A. Hussain, Preparation and characterization of PVA/nanocellulose/Ag nanocomposite films for antimicrobial food packaging, Carbohydr. Polym. 184 (2018) 453–464, https://doi.org/10.1016/j.carbpol.2017.12.068.
[5] P. Cheng, X. Wang, Y. Liu, C. Kong, N. Liu, Y. Wan, Q. Guo, K. Liu, Z. Lu, M. Li, D. Wang, Ag nanoparticles decorated PVA-co-PE nanofiber-based membrane with antifouling surface for highly efficient inactivation and interception of bacteria, Appl. Surf. Sci. 506 (2020), https://doi.org/10.1016/j.apsusc.2019.144664.
[6] M. Banerjee, S. Mallick, A. Paul, A. Chattopadhyay, S.S. Ghosh, Heightened reactive oxygen species generation in the antimicrobial activity of a three component iodinated chitosan-silver nanoparticle composite, Langmuir 26 (2010) 5901–5908, https://doi.org/10.1021/la9038528.
[7] A.P. B. Hilgenberg, L. Vossebein, in Antimicrobial Textiles, Woodhead Publishing (2016) 7-18, https://doi.org/10.1016/b978-0-08-100576-7.09002-7.
[8] A. Gao, H. Zhang, G. Sun, K. Xie, A. Hou, Light-induced antibacterial and UV-protective properties of polyamide 56 biomaterial modified with anthraquinone and benzophenone derivatives, Mater. Des. 130 (2017) 215–222, https://doi.org/10.1016/j.matdes.2017.05.071.
[9] N. Allen, Photocatalysis: Science and Technology: M. Kaneko, I. Okura (Eds.); Springer, Heidelberg, ISBN 3-540-43473-9, J. Photochem. Photobiol. A Chem. 160 (2003) 225, https://doi.org/10.1016/S1010-6030(03)00234-X.
[10] K.H. Hong, N. Liu, G. Sun, UV-induced graft polymerization of acrylamide on cellulose by using immobilized benzophenone as a photo-initiator, Eur. Polym. J. 45 (2009) 2443–2449, https://doi.org/10.1016/j.eurpolymj.2009.04.026.
[11] Y. Si, Z. Zhang, W. Wu, Q. Fu, K. Huang, N. Nitin, B. Ding, G. Sun, Daylight-driven rechargeable antibacterial and antiviral nanofibrous membranes for bioprotective applications, Sci. Adv. 4 (2018) 5931, https://doi.org/10.1126/sciadv.aar5931.
[12] K.H. Hong, G. Sun, Photoactive antibacterial cotton fabrics treated by 3,3′,4,4′-benzophenonetetracarboxylic dianhydride, Carbohydr. Polym. 84 (2011) 1027–1032, https://doi.org/10.1016/j.carbpol.2010.12.062.
[13] C. Zhao, G. Sun, Catalytic Actions of Sodium Salts in Direct Esterification of 3,3′4,4′-Benzophenone Tetracarboxylic Acid with Cellulose, Ind. Eng. Chem. Res. 54 (2015) 10553–10559, https://doi.org/10.1021/acs.iecr.5b02308.
[14] A. Hou, G. Feng, J. Zhuo, G. Sun, UV Light-Induced Generation of Reactive Oxygen Species and Antimicrobial Properties of Cellulose Fabric Modified by 3,3',4,4'-Benzophenone Tetracarboxylic Acid, ACS Appl. Mater. Interfaces 7 (2015) 27918–27924, https://doi.org/10.1021/acsami.5b09993.
[15] Y.J. Choi, T.J. Luo, Self-Assembly of Silver-Aminosilica Nanocomposites through Silver Nanoparticle Fusion on Hydrophobic Surfaces, ACS applied materials & interfaces 1 (2009) 2778–2784, https://doi.org/10.1021/am900524j.
[16] R. Southward, C. Boggs, D. Thompson, A. Clair, Synthesis of Surface-Metallized Polyimide Films via in Situ Reduction of (Perfluoroalkanoato)silver(I) Complexes in a Poly(amic acid) Precursor, Chemistry of Materials - CHEM MATER 10 (1998), https://doi.org/10.1021/cm9707770.
[17] B. Carlberg, L.L. Ye, J. Liu, Surface-confined synthesis of silver nanoparticle composite coating on electrospun polyimide nanofibers, Small 7 (2011) 3057–3066, https://doi.org/10.1002/smll.201101172.
[18] S. Yang, P. Lei, Y. Shan, D. Zhang, Preparation and characterization of antibacterial electrospun chitosan/poly (vinyl alcohol)/graphene oxide composite nanofibrous membrane, Appl. Surf. Sci. 435 (2018) 832–840, https://doi.org/10.1016/j.apsusc.2017.11.191.
[19] T. Galya, V. Sedlařík, I. Kuřitka, R. Novotný, J. Sedlaříková, P. Sáha, Antibacterial poly(vinyl alcohol) film containing silver nanoparticles: Preparation and characterization, J. Appl. Polym. Sci. 110 (2008) 3178–3185, https://doi.org/10.1002/app.28908.
[20] C.Q. Yang, W. Xilie, Formation of Cyclic Anhydride Intermediates and Esterification of Cotton Cellulose by Multifunctional Carboxylic Acids: An Infrared Spectroscopy Study, Textile Research Journal 66 (1996) 595–603, https://doi.org/10.1177/004051759606600908.
[21] C.Q. Yang, Infrared spectroscopy studies of the cyclic anhydride as the intermediate for the ester crosslinking of cotton cellulose by polycarboxylic acids. I.

Identification of the cyclic anhydride intermediate, Journal of Polymer Science Part A: Polymer Chemistry 31 (1993) 1187–1193, https://doi.org/10.1002/pola.1993.080310514.
[22] A.T. Hang, B. Tae, J.S. Park, Non-woven mats of poly(vinyl alcohol)/chitosan blends containing silver nanoparticles: Fabrication and characterization, Carbohydr. Polym. 82 (2010) 472–479, https://doi.org/10.1016/j.carbpol.2010.05.016.
[23] C. Sharma, N.K. Bhardwaj, Fabrication of natural-origin antibacterial nanocellulose films using bio-extracts for potential use in biomedical industry, Int. J. Biol. Macromol. 145 (2020) 914–925, https://doi.org/10.1016/j.ijbiomac.2019.09.182.
[24] H. Wu, Y. Lei, R. Zhu, M. Zhao, J. Lu, D. Xiao, C. Jiao, Z. Zhang, G. Shen, S. Li, Preparation and characterization of bioactive edible packaging films based on pomelo peel flours incorporating tea polyphenol, Food Hydrocolloids 90 (2018) 41–49, https://doi.org/10.1016/j.foodhyd.2018.12.016.
[25] S. Shankar, X. Teng, G. Li, J.-W. Rhim, Preparation, characterization, and antimicrobial activity of gelatin/ZnO nanocomposite films, Food Hydrocolloids 45 (2015) 264–271, https://doi.org/10.1016/j.foodhyd.2014.12.001.
[26] H. Wu, Y. Lei, J. Lu, R. Zhu, D. Xiao, C. Jiao, R. Xia, Z. Zhang, G. Shen, Y. Liu, S. Li, M. Li, Effect of citric acid induced crosslinking on the structure and properties of potato starch/chitosan composite films, Food Hydrocolloids 97 (2019), https://doi.org/10.1016/j.foodhyd.2019.105208.
[27] O. Gul, F.T. Saricaoglu, A. Besir, I. Atalar, F. Yazici, Effect of ultrasound treatment on the properties of nano-emulsion films obtained from hazelnut meal protein and clove essential oil, Ultrason. Sonochem. 41 (2018) 466–474, https://doi.org/10.1016/j.ultsonch.2017.10.011.
[28] N. Liu, G. Sun, Production of Reactive Oxygen Species by Photoactive Anthraquinone Compounds and Their Applications in Wastewater Treatment, Ind. Eng. Chem. Res. 50 (2011) 103–109, https://doi.org/10.1021/ie101423v.
[29] S. Mallakpour, S. Mansourzadeh, Sonochemical synthesis of PVA/PVP blend nanocomposite containing modified CuO nanoparticles with vitamin B1 and their antibacterial activity against Staphylococcus aureus and Escherichia coli, Ultrason. Sonochem. 43 (2018) 91–100, https://doi.org/10.1016/j.ultsonch.2017.12.052.
[30] Y. Qin, Y. Liu, X. Zhang, J. Liu, Development of active and intelligent packaging by incorporating betalains from red pitaya (Hylocereus polyrhizus) peel into starch/polyvinyl alcohol films, Food Hydrocolloids 100 (2020), https://doi.org/10.1016/j.foodhyd.2019.105410.
[31] L. Hu, A. Hou, K. Xie, A. Gao, Light-Induced Production of Reactive Oxygen Species by a Novel Water-Soluble Benzophenone Derivative Containing Quaternary Ammonium Groups and Its Assembly on the Protein Fiber Surface, ACS Appl Mater Interfaces 11 (2019) 26500–26506, https://doi.org/10.1021/acsami.9b07992.
[32] H. Gruen, H. Görner, Photoreduction of 2-methyl-1-nitro-9,10-anthraquinone in the presence of 1-phenylethanol, Photochemical & photobiological sciences : Official journal of the, European Photochemistry Association and the European Society for Photobiology 7, 2008, pp. 1344–1352.
[33] S. Yi, Y. Zou, S. Sun, F. Dai, Y. Si, G. Sun, Rechargeable Photoactive Silk-Derived Nanofibrous Membranes for Degradation of Reactive Red 195, ACS Sustainable Chemistry & Engineering 7 (2018) 986–993, https://doi.org/10.1021/acssuschemeng.8b04646.
[34] Y. Zhao, Y. Zhou, X. Wu, L. Wang, L. Xu, S. Wei, A facile method for electrospinning of Ag nanoparticles/poly (vinyl alcohol)/carboxymethyl-chitosan nanofibers, Appl. Surf. Sci. 258 (2012) 8867–8873, https://doi.org/10.1016/j.apsusc.2012.05.106.
[35] Z. Zhang, Y. Wu, Z. Wang, X. Zou, Y. Zhao, L. Sun, Fabrication of silver nanoparticles embedded into polyvinyl alcohol (Ag/PVA) composite nanofibrous films through electrospinning for antibacterial and surface-enhanced Raman scattering (SERS) activities, Mater. Sci. Eng. C Mater. Biol. Appl. 69 (2016) 462–469, https://doi.org/10.1016/j.msec.2016.07.015.
[36] X. Sun, C. Lu, Y. Liu, W. Zhang, X. Zhang, Melt-processed poly(vinyl alcohol) composites filled with microcrystalline cellulose from waste cotton fabrics, Carbohydr. Polym. 101 (2014) 642–649, https://doi.org/10.1016/j.carbpol.2013.09.088.
[37] A. Hamza, E.D. Alhtheal, A. Shakir, Enhancement the Efficiency of ZnOnanofiber mats antibacterial Using Novel PVA/Ag nanoparticles, Energy Procedia 119 (2017) 615–621, https://doi.org/10.1016/j.egypro.2017.07.087.
[38] F. Wahid, F.P. Wang, Y.Y. Xie, L.Q. Chu, S.R. Jia, Y.X. Duan, L. Zhang, C. Zhong, Reusable ternary PVA films containing bacterial cellulose fibers and epsilon-polylysine with improved mechanical and antibacterial properties, Colloids Surf. B. Biointerfaces 183 (2019) 110486, , https://doi.org/10.1016/j.colsurfb.2019.110486.
[39] S. Shankar, N. Tanomrod, S. Rawdkuen, J.W. Rhim, Preparation of pectin/silver nanoparticles composite films with UV-light barrier and properties, Int. J. Biol. Macromol. 92 (2016) 842–849, https://doi.org/10.1016/j.ijbiomac.2016.07.107.
[40] A. Hou, G. Sun, Multifunctional finishing of cotton with 3,3',4,4'-benzophenone tetracarboxylic acid: functional performance, Carbohydr. Polym. 96 (2013) 435–439, https://doi.org/10.1016/j.carbpol.2013.04.015.
[41] E. Fortunati, F. Luzi, D. Puglia, A. Terenzi, M. Vercellino, L. Visai, C. Santulli, L. Torre, J.M. Kenny, Ternary PVA nanocomposites containing cellulose nanocrystals from different sources and silver particles: part II, Carbohydr. Polym. 97 (2013) 837–848, https://doi.org/10.1016/j.carbpol.2013.05.015.
[42] J. George, V.A. Sajeevkumar, K.V. Ramana, S.N. Sabapathy, Siddaramaiah, Augmented properties of PVA hybrid nanocomposites containing cellulose nanocrystals and silver nanoparticles, J. Mater. Chem. 22 (2012) 22433–22439, https://doi.org/10.1039/c2jm35235d.
[43] Y. Ma, S. Li, T. Ji, W. Wu, D.E. Sameen, S. Ahmed, W. Qin, J. Dai, Y. Liu, Development and optimization of dynamic gelatin/chitosan nanoparticles incorporated with blueberry anthocyanins for milk freshness monitoring, Carbohydr. Polym. 247 (2020), https://doi.org/10.1016/j.carbpol.2020.116738.
[44] K. Vimala, M.M. Yallapu, K. Varaprasad, N.N. Reddy, S. Ravindra, N.S. Naidu, K.M. Raju, Fabrication of Curcumin Encapsulated Chitosan-PVA Silver Nanocomposite Films for Improved Antimicrobial Activity, J. Biomater. Nanobiotechnol. 02 (2011) 55–64, https://doi.org/10.4236/jbnb.2011.21008.
[45] M.T. Ramesan, A. George, P. Jayakrishnan, G. Kalaprasad, Role of pumice particles in the thermal, electrical and mechanical properties of poly(vinyl alcohol)/poly (vinyl pyrrolidone) composites, J. Therm. Anal. Calorim. 126 (2) (2016) 511–519, https://doi.org/10.1007/s10973-016-5507-6.
[46] A. Mittal, S. Garg, D. Kohli, M. Maiti, A.K. Jana, S. Bajpai, Effect of cross linking of PVA/starch and reinforcement of modified barley husk on the properties of composite films, Carbohydr. Polym. 151 (2016) 926–938, https://doi.org/10.1016/j.carbpol.2016.06.037.
[47] H. Cui, S. Siva, L. Lin, Ultrasound processed cuminaldehyde/2-hydroxypropyl-beta-cyclodextrin inclusion complex: Preparation, characterization and antibacterial activity, Ultrason. Sonochem. 56 (2019) 84–93, https://doi.org/10.1016/j.ultsonch.2019.04.001.
[48] R. Bryaskova, D. Pencheva, G.M. Kale, U. Lad, T. Kantardjiev, Synthesis, characterisation and antibacterial activity of PVA/TEOS/Ag-Np hybrid thin films, J. Colloid Interface Sci. 349 (2010) 77–85, https://doi.org/10.1016/j.jcis.2010.04.091.
[49] C. Wu, Y. Li, Y. Du, L. Wang, C. Tong, Y. Hu, J. Pang, Z. Yan, Preparation and characterization of konjac glucomannan-based bionanocomposite film for active food packaging, Food Hydrocolloids 89 (2019) 682–690, https://doi.org/10.1016/j.foodhyd.2018.11.001.
[50] P.J. Babu, M. Doble, A.M. Raichur, Silver oxide nanoparticles embedded silk fibroin spuns: Microwave mediated preparation, characterization and their synergistic wound healing and anti-bacterial activity, J. Colloid Interface Sci. 513 (2018) 62–71, https://doi.org/10.1016/j.jcis.2017.11.001.
[51] H. Haghighi, S.K. Leugoue, F. Pfeifer, H.W. Siesler, F. Licciardello, P. Fava, A. Pulvirenti, Development of antimicrobial films based on chitosan-polyvinyl alcohol blend enriched with ethyl lauroyl arginate (LAE) for food packaging applications, Food Hydrocolloids 100 (2020), https://doi.org/10.1016/j.foodhyd.2019.105419.
[52] H. Haghighi, S. Biard, F. Bigi, R. De Leo, E. Bedin, F. Pfeifer, H.W. Siesler, F. Licciardello, A. Pulvirenti, Comprehensive characterization of active chitosan-gelatin blend films enriched with different essential oils, Food Hydrocolloids 95 (2019) 33–42, https://doi.org/10.1016/j.foodhyd.2019.04.019.
[53] T. Liang, G. Sun, L. Cao, J. Li, L. Wang, A pH and NH3 sensing intelligent film based on Artemisia sphaerocephala Krasch. gum and red cabbage anthocyanins anchored by carboxymethyl cellulose sodium added as a host complex, Food Hydrocolloids 87 (2019) 858–868, https://doi.org/10.1016/j.foodhyd.2018.08.028.
[54] A. Cano, M. Cháfer, A. Chiralt, C. González-Martínez, Development and characterization of active films based on starch-PVA, containing silver nanoparticles, Food Packaging and Shelf Life 10 (2016) 16–24, https://doi.org/10.1016/j.fpsl.2016.07.002.
[55] R. Andretta, C.L. Luchese, I.C. Tessaro, J.C. Spada, Development and characterization of pH-indicator films based on cassava starch and blueberry residue by thermocompression, Food Hydrocolloids 93 (2019) 317–324, https://doi.org/10.1016/j.foodhyd.2019.02.019.
[56] S.F. Hosseini, Z. Nahvi, M. Zandi, Antioxidant peptide-loaded electrospun chitosan/poly(vinyl alcohol) nanofibrous mat intended for food biopackaging purposes, Food Hydrocolloids 89 (2019) 637–648, https://doi.org/10.1016/j.foodhyd.2018.11.033.
[57] C. Fan, R. Cui, W. Lu, H. Chen, M. Yuan, Y. Qin, Effect of high pressure treatment on properties and nano–Ag migration of PLA-based food packaging film, Polym. Test. 76 (2019) 73–81, https://doi.org/10.1016/j.polymertesting.2019.03.005.
[58] S. Boughriba, N. Souissi, M. Jridi, S. Li, M. Nasri, Thermal, mechanical and microstructural characterization and antioxidant potential of Rhinobatos cemiculus gelatin films supplemented by titanium dioxide doped silver nanoparticles, Food Hydrocolloids 103 (2020), https://doi.org/10.1016/j.foodhyd.2020.105695.
[59] U. Siripatrawan, B.R. Harte, Physical properties and antioxidant activity of an active film from chitosan incorporated with green tea extract, Food Hydrocolloids 24 (2010) 770–775, https://doi.org/10.1016/j.foodhyd.2010.04.003.
[60] I. Basha, S. Ghosh, K. Vinothkumar, B. Ramesh, P.H.P. Kumari, K.V.M. Mohan, E. Sukumar, Fumaric acid incorporated Ag/agar-agar hybrid hydrogel: A multifunctional avenue to tackle wound healing, Mater. Sci. & Eng. C (2020) 111, https://doi.org/10.1016/j.msec.2020.110743.
[61] J.R. Nakkala, R. Mata, K. Raja, V. Khub Chandra, S.R. Sadras, Green synthesized silver nanoparticles: Catalytic dye degradation, in vitro anticancer activity and in vivo toxicity in rats, Mater. Sci. Eng. C Mater. Biol. Appl. 91 (2018) 372–381, https://doi.org/10.1016/j.msec.2018.05.048.
[62] L. Zhang, L. Li, L. Wang, J. Nie, G. Ma, Multilayer electrospun nanofibrous membranes with antibacterial property for air filtration, Appl. Surf. Sci. 515 (2020), https://doi.org/10.1016/j.apsusc.2020.145962.